

Fracture Initiation Toughness and Propagation Toughness of Laurentian Granite Rock

F. Lu¹, R. Chen^{1,2}, L. Lu¹ and K. Xia²

¹ *National University of Defense Technology, Changsha, P.R. China;*

² *University of Toronto, Toronto, Canada*

A new method is proposed to measure initiation and propagation toughness of Laurentian granite (LG). This method is based on three point bending tests at high loading rates, performed using a modified Split Hopkinson Pressure Bar (SHPB). The semi-circular bend (SCB) sample is used in our experiment. In addition, a laser displacement meter is used to measure the crack surface opening displacement (CSOD) of the specimen directly. A two-dimensional numerical simulation is carried out with ANSYS to determine the initiation fracture toughness with the experimental recorded loading history of the sample. From CSOD, the residual kinetic energy of the sample can be estimated, together with the estimation of the total consumed energy with stress waves recorded, the average propagation fracture energy and the propagation toughness can be calculated. Three loading rates are achieved in our tests and both the initiation toughness and propagation toughness are rate depend.

1 INTRODUCTION

Dynamic fracture plays a vital role in geophysics applications and in many engineering applications. Most of the existing experimental fracture studies of rocks are carried out under static loading conditions. It is thus highly desirable to develop methods to measure rock's dynamic fracture parameters. A few attempts have been made to measure the dynamic initiation fracture toughness of rocks in the literatures using split Hopkinson pressure bars (SHPB). For example, Zhang et al. applied SHPB to measure the dynamic initiation fracture toughness of a rock [1, 2]. In these attempts, the inertial effect associated with the stress wave loading as demonstrated by Böhme and Kalthoff [3] was ignored. This leads to concerns on the reliability of the experimental results. One way to remedy this inadequacy is to combine experimental measurements with numerical simulations [4]. This is a rather tedious process, especially when the number of tests is significant. Recently, Owen et al. observed that in Hopkinson tension bars tests, the stress intensity factors (SIF) obtained by directly measuring the crack tip opening are consistent with those calculated by using the quasi-static equation when the dynamic stress equilibrium of the specimen is roughly achieved [5]. This concept was used by Weerasooriya et al. in the measurement of dynamic fracture toughness of ceramics employing four-point bend specimens with SHPB [6].

Parameters other than the initiation toughness, such as fracture energy and fracture velocity are also needed to characterize the material dynamic fracture responses. The fracture energy or the fracture propagation toughness is especially

important because they are directly related to the energy consumption during material dynamic failures. To our best knowledge, there is only one attempt on the dynamic propagation toughness measurement of rocks [7], where a chain of strain gauges was used to measure the strains associated with fracture propagation. For dynamic fractures, the shrinkage of the domain of small scale yielding may leads to significant error for methods based only on the singular term of the stress field (e.g., strain gauge method, caustics) [8]. Indeed, six terms of expansion of the stress fields is needed to fit the photoelastic fringe patterns [9]. However, an energy based method is capable of avoiding that problem.

Tang and Xu tried to measure crack surface opening displacement (CSOD) using a synchronous line white light [10]. They used the turning point of the CSOD history as the fracture initiation time. Zhang et al. used the Moiré method to monitor the CSOD of short rod (SR) specimens, and the authors claimed that the peak point of the opening velocity curve obtained from CSOD corresponds to the onset of fracture [1]. However, these arguments were not rigorously verified. In 1996, Ramesh and Kelkar adopted a line laser as the light source to measure the velocity history of flyer in planer impact [11]. In this study, a laser gap gauge (LGG), which is based on the current line laser technique, is used to monitor the CSOD of the semi-circular bend (SCB) specimen.

The idea of measuring fracture energy is as follows. From the CSOD measurements, angular velocities of the two rotating fragments produced by the dynamic fracture can be estimated. With the residual kinetic energy and total energy consumption deduced from the strain gauge signals, not only the initiation fracture toughness, but also the propagation fracture toughness are obtained. The similar method was first attempted by Zhang et al., who used a high-speed camera to estimated the fragment velocities [2]. The fracture toughness was not explicitly presented in their work nore information on the fracture velocity was obtained using their technique. We will show that using the CSOD data with LGG, we can also determine the completion time of the fracture. Because we have achieved dynamic force balance in all of our tests, the peak in the loading history corresponds to the onset time of the fracture. The total fracture growth length is measured from the sample geometry. We can thus calculate the averaged fracture velocity for the SCB rock specimen.

The experiment setups, including LGG are presented in Sec. II. The principles of the measurement are detailed in Sec. III, including the calibration of the LGG, the method to determine the fracture initiation toughness, the fracture energy, the fracture propagation toughness, and the fracture velocity. Sec. IV illustrates the application of this method to LG. Main conclusions are summarized in Sec. V.

2 EXPERIMENT SETUPS

Since rock materials are weaker in tension, fracture tests are usually done with compressive loadings to avoid pre-mature failure due to gripping. In this spirit,

Chong and Kuruppu [12] proposed a SCB specimen with a single edge notch to measure rock fracture toughness. The radius of the specimen is denoted as R , the depth of the notch is a , the thickness is B and the span of the supporting pins is S . The thickness of the notch is around 1 mm. The force applied on one side of the sample is P_1 and on the other side is P_2 , which is split by the two supporting points as $P_2/2$.

A 25 mm diameter SHPB system is used in the study to apply dynamic loading (Fig. 1). The bars are made from Maraging steel, with a high yielding strength of 2.5 GPa. The length of the striker bar is 200 mm. The incident (input) bar is 1500 mm long and the strain gauge station is 787 mm away from the impact end of the bar. The transmitted (output) bar is 1000 mm long and the strain gauge station is 522 mm away from the specimen. The striker bar is launched by a low pressure gas gun to impact on the incident bar, resulting in an incident stress wave. The incident pulse propagates along the incident bar before it hit the sample, leading to reflected stress wave and transmitted stress wave. An eight-channel Sigma digital oscilloscope by Nicolet is used to record and store the strain signals collected from the Wheatstone bridge circuits after amplification. Denoting the incident wave, reflected wave and transmitted wave by ε_i , ε_r , and ε_t , the loading histories of specimen induced by the SHPB are [13]:

$$P_1 = A_0 E_0 (\varepsilon_i + \varepsilon_r), P_2 = A_0 E_0 \varepsilon_t \quad (1)$$

where E_0 is Young's modulus of the bar material and A_0 is the cross-sectional area of the bar.

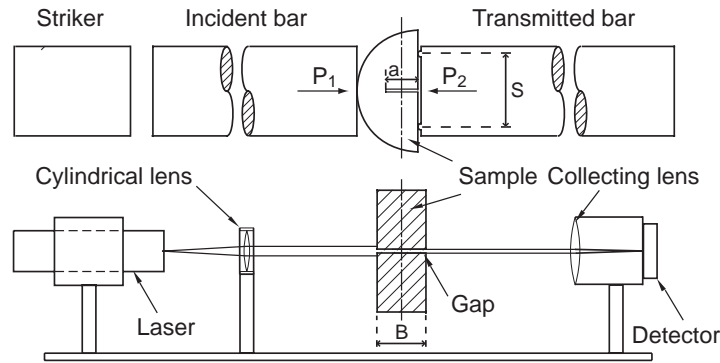


Fig. 1. Schematics of SHPB and LGG

A schematic diagram of the experimental configuration for the LGG system is shown in Fig. 1. The LGG system is composed of a line laser, a cylindrical lens, a collector lens and a light detector. A diode line laser generator produces a line laser operating at 670 nm with 5 mW output power. Superior optical design of this system yields a large field depth and minimal variations in its thickness across the length of the generated line. The line is as thin as 30 μm at 185 mm away from the generator, and the angle of the fan-shaped laser sheet is 5°. The

cylindrical lens is used to achieve a parallel laser sheet. The high performance multilayer AR coatings have an average reflectance of less than 0.5 % (per surface) across the operational wavelength range (650-1050 nm). The light detecting system consists of a collecting lens and a photodiode light detector. The collecting lens focuses the incoming laser light into the photodiode detector, which is placed near its focal point. A filter placed in front of the detector window ensures single color operation at the wave length of 670 nm, matching that of the laser. The photodiode detector output is pre-amplified and the optoelectronics and the preamplifier together have a bandwidth of 1.5 MHz. The output voltage of the detector is proportional to the total amount of laser light collected. The whole system has a noise level less than 0.4 mV.

The LGG system monitors the change of the width of the laser sheet that passes through a gap. In SHPB tests of SCB, LGG is mounted perpendicular to the bar axis (Fig. 1). The specimen blocks the laser sheet except for the notched portion in the center of the specimen. As the notch opens up, the amount of light passing through increases. This will lead to higher voltage output from the detector. By recording the detector output during the test, one can monitor the variation of CSOD. To do so, we should first calibrate LGG to convert the voltage readings to the width measurements of the laser sheet.

3 MEASUREMENT TECHNIQUES AND PRINCIPLES

3.1 CALIBRATION OF THE LGG

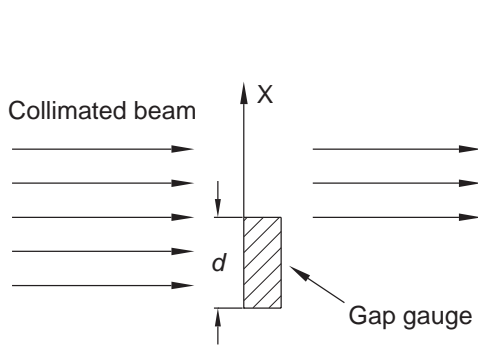


Fig. 2. Sketch of static calibration principle.

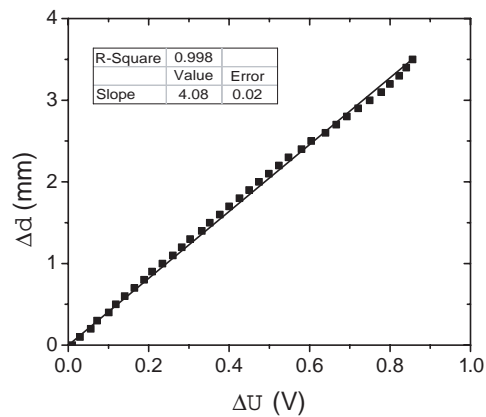


Fig. 3. A typical static calibration curve.

The calibration of the LGG is done under both static and dynamic conditions. For static calibration, a set of high quality gap gauges with thicknesses from 1 mm to 10 mm at a step of 0.1 mm are used to block the line laser sheet (Fig. 3). When a gauge of given thickness is transported into the laser blocking location, a step variation of the output voltage is induced and recorded. Following this procedure, a curve between the output voltage and the thickness of the gap gauge is obtained

as shown in Fig. 3. The curve exhibits good linearity, indicating the high uniformity of the laser sheet. A linear fitting is thus used between the gap gauge thickness d and detector output ΔU :

$$\Delta d = k\Delta U \quad (2)$$

where the k is the calibration parameter of the LGG system. We denote the standard deviation as σ , and the error propagation can be calculated by eq. (2) as $\sigma_{\Delta d} / \Delta d = \sqrt{(\sigma_x / k)^2 + (\sigma_{\Delta U} / \Delta U)^2}$. Where $\sigma_k = 0.03$ is the error of the linear fitted parameter as shown in Fig. 3, and the noise of the output voltage σ_k is 0.4 mv. As an example, if the output voltage is $\Delta U = 0.25$ V, the percentage error of the displacement measurement is around 0.7 %.

3.2 DYNAMIC FORCE BALANCE

The pulse shaper technique is employed to achieve dynamic force balance in the specimen during the experiment (i.e., $P_1 = P_2$). This technique was recently discussed in detail by Frew et al. for SHPB compressive tests of brittle materials [14]. In the traditional SHPB test, the incident wave with a sharp rising edge can initiate unwanted damages upon hitting the sample. Consequently, the forces on both sides of the specimen will not be the same. This will result in problems in the data interpretation [6]. We use a C11000 copper disc to shape the incident wave from the rectangle shape to a sinusoidal wave. In addition, a rubber disc is tipped in front of the copper shaper to further slow down the rising edge of the incident pulse. This method is called the combined pulse shaping technique.

Fig. 4 shows the forces on both ends of the specimen in a typical test. From Eq. 1, the dynamic force on one side of the specimen P_1 is proportional to the sum of the incident (In) and reflected (Re) stress waves, and the dynamic force on the other side of the specimen P_2 is proportional to the transmitted (Tr) stress wave. For SCB tests, P_2 is equally supported by two pins. It can be seen from Fig. 4 that the dynamic forces on both sides of the specimens are almost identical during the whole dynamic loading period. The inertial effects are thus eliminated because there is no global force difference in the specimen to induce inertial forces. Consequently, the inertial effects can be ignored and we can then treat the problem using quasi-static analysis [6].

3.3 FRACTURE VELOCITY

Fig. 5 shows a typical loading history and the corresponding CSOD history for a test. The loading history plotted is for P_2 . Because the dynamic force balance is achieved, the peak point of the loading corresponds to the fracture initiation in the specimen, as in a quasi-static experiment. The peak point of the loading history is denoted by A. With the differentiation of the CSOD history we can get the crack surface opening velocity (CSOV) history. B is the cross point of the CSOV history and the straight line of $v = 11.28$ m/s, which is the terminal velocity linear

fitted by the CSOD history. The two vertical lines passing through points A and B in Fig. 5 divide the whole deformation period into three stages, denoted by I, II, and III. We believe that in stage I the crack opens up elastically, in stage II the crack propagates dynamically, and in stage III the dynamic fracture separate the sample into two pieces and the two fragments are flying away from each other.

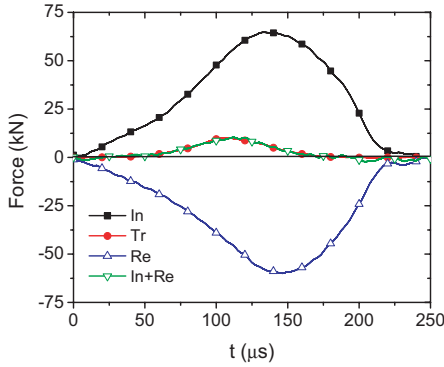


Fig. 4. Dynamic force balance check of SHPB tests of SCB specimen.

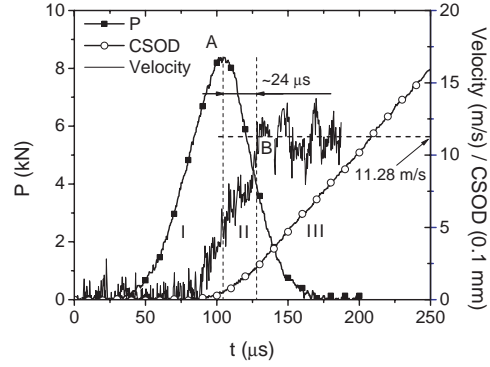


Fig. 5. Typical Loading history and CSOD history of the SCB specimen tested in SHPB.

As shown in Fig. 5, the crack propagation process lasts about $\Delta t = 24 \mu\text{s}$. Knowing that the crack distance $L_s = R - a = 16 \text{ mm}$ in the test, we can estimate the average crack growth velocity v_f , which is about 670 m/s. The fragments rotate with the axial along the loading point A, as shown in Fig. 6. The linear velocity of the two rotating fragments at the LGG point is identified as the slope of the CSOD curve after point B. With the distance between the LGG and the rotating axis Δl , the angular velocity $\omega = v/2/\Delta l$ can be estimated.

3.4 INITIATION FRACTURE TOUGHNESS AND LOADING RATE

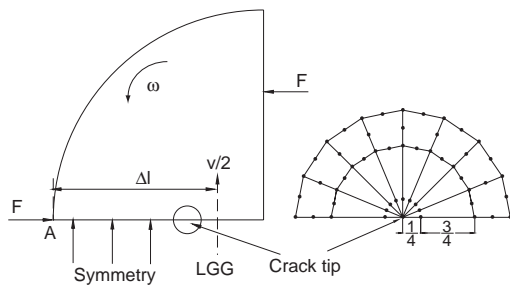


Fig. 6. Quarter point element on the crack tip

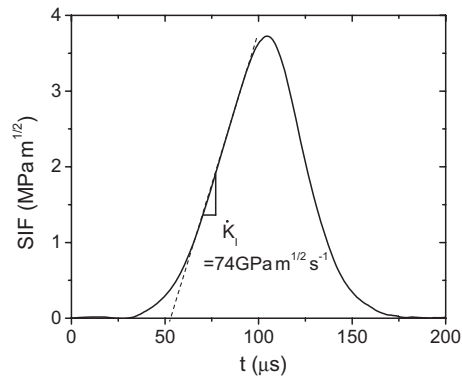


Fig. 7. The dynamic SIF history and the determination of the loading rate.

Based on the ASTM standard E399-90 for rectangular three-point bending sample, we propose a similar equation for calculating the mode-I fracture SIF for the SCB specimen:

$$K_I(t) = \frac{P(t)S}{BR^{3/2}} \cdot Y\left(\frac{a}{R}\right) \quad (3)$$

where $P(t)$ is the time-varying load, and $Y(a/R)$ is a function of dimensionless crack length (a/R). For a given sample dimension, the numerical value of $Y(a/R)$ can be calculated using the finite element software ANSYS.

As mentioned earlier, we guarantee identical forces applied on both side of the sample during our SHPB tests, i.e, $F = P_1/2 = P_2/2 = P/2$ (Fig. 6). The inertial effects are eliminated because there is no global force difference in the specimen to induce inertial forces [6]. The goal of the simulation is to relate the far-field loading to the local SIF of the crack tip for the given specimen geometries. This process is called numerical calibration. Taking advantage of the symmetry of the problem, half-crack model is used to construct the finite element model. PLAIN82 (eight-node) element is used in the analysis. To better simulate the stress singularity of $r^{1/2}$ near the crack tip (r is the radius to the crack tip), 1/4 nodal element (singular element) [15] is applied to the vicinity of the crack tip in the mesh of the finite element model (Fig. 6). We use Young's modulus of 92 GPa and the Poisson's ratio of 0.21 for LG [16]. The load is set as the boundary stresses at the left and right edge of the model plate while the lower edge of the model has the symmetry boundary condition. The resulting loading at the main crack is mode I. For given load P , the SIF K_I can be obtained and the parameter $Y(a/R)$ is calculated as:

$$Y\left(\frac{a}{R}\right) = \frac{K_I BR^{3/2}}{PS} \quad (4)$$

The peak point of the loading P_{\max} corresponds to the initiation fracture toughness K_{IC}^d using Eq. 3.

Fig. 7 shows the variation of SIF with time for a typical test for a specimen with 4 mm depth notch. There is a regime of approximately linear variation of SIF with time from 60 μ s to 95 μ s. The slope of this region is determined from a least squares fit, shown as a dashed line in the figure and this slope is used as the fracture loading rate, which is $\dot{K}_I = 74 \text{ GPa m}^{1/2} \text{ s}^{-1}$.

3.5 PROPAGATION FRACTURE ENERGY AND TOUGHNESS

We used an energetic method to calculate propagation fracture energy and fracture toughness. The similar method was used by Zhang et al., who used a

high-speed camera to estimated the fragment residual velocities [2]. The elastic energy carried by the stress wave is:

$$W = \frac{1}{2} \int_0^t E_0 \varepsilon^2 A_0 C_0 d\tau \quad (5)$$

The total energy absorbed by the specimen then is $\Delta W = W_i - W_r - W_t$, where W_i , W_r and W_t are the energy carried by the incident, reflected and transmitted wave respectively. Part of the total energy absorbed is used to create new crack surfaces, called total fracture energy, the other part remains in the fragments in the form of residue kinetic energy is $\Delta W = W_G + K$, where W_G is the total fracture energy, and K is the kinetic energy of fragments. Denoting the mass moment of inertia with axis A (shown in Fig. 6) as I , the total kinetic energy for the two fragments is $K = I\omega^2/2$, where the fragment angular velocity ω is estimated using the CSOD data measured with LGG as mentioned earlier. The average propagation fracture energy is $G_c = W_G / A_c$, where A_c is the area of the crack surface created. The average dynamic propagation fracture toughness is:

$$K_{IC}^{dp} = \sqrt{G_c E} \quad (6)$$

where E is the Young's modulus of LG. In this equation, we assume plain stress condition.

4 APPLICATION TO LAURENTIAN GRANITE (LG)

To demonstrate the feasibility and flexibility of the dynamic loading with the new method, we have performed full SHPB tests on LG. LG is from the Laurentian region of Grenville province of the Precambrian Canadian Shield, north of St. Lawrence and north-west of Quebec City, Canada. The mineral grain size of Laurentian granite varies from 0.2 to 2 mm with the average quartz grain size of 0.5 mm and the average feldspar grain size of 0.4 mm, with feldspar being the dominant mineral (60 %) followed by quartz (33 %). Biotite grain size is of the order of 0.3 mm and constitutes 3~5 % of this rock. As we see, LG is fine-grained rock. This fact allows us to use relatively small specimens in the test while ensuring valid testing conditions.

Rock cores with a nominal diameter of 40 mm are drilled from LG blocks. They are then sliced to get disks with an average thickness of 16 mm. A circular diamond saw is used to first split the disk and then to make a 4 mm depth notch on the semi circular sample for bending test. The recovered sample is clearly split into two pieces. For our samples where a is around 4 mm, $Y(a/R)$ is 0.086 for the fixed $S = 20.1$ mm. This value is then substitute into Eq. 3 with P_{max} to calculate the dynamic inciate fracture toughness. Other parameters are determined with methods discussed in the previous section.

Fig. 8 shows the measured initiation and propagation fracture toughness with different loading rates. It can be seen that both the initiation and the propagation fracture toughnesses increase with the loading rate. The linear fits for both toughnesses show similar slope, indicating similar rate effect for these two types of toughness. For our data set, the increase of propagation fracture toughness with fracture velocity is shown in Fig. 9. At the high fracture velocity (~ 850 m/s), the fracture toughness value is $7.098 \text{ MPa m}^{1/2}$, twice of those for fractures at slower fracture velocities of $290\sim 293$ m/s.

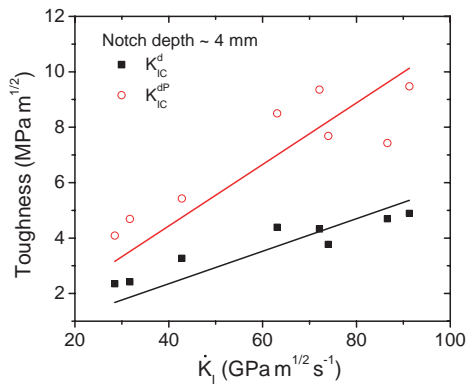


Fig. 8. The effect of loading rate on the fracture toughness

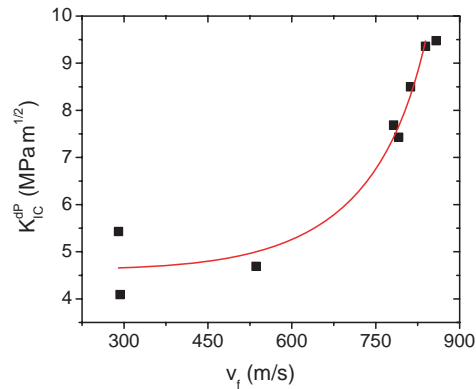


Fig. 9. The variation of dynamic propagation fracture toughness with fracture velocity

5 CONCLUSION

An innovative technique using SCB specimen to measure the dynamic mode-I initiation fracture toughness, averaged dynamic fracture, average propagation toughness, and average fracture velocity of brittle materials in SHPB tests is proposed. In this technique, we developed a LGG system to measure the CSOD history and from which, fracture energy is determined with an energetic consideration. The averaged fracture velocity is also determined under the condition that dynamic force equilibrium is achieved during the SHPB test. LG is tested to demonstrate the feasibility and flexibility of this method. Both the initiation toughness and propagation toughness are loading rate dependent. The propagation toughness is larger than the initiation toughness for a given test. The propagation fracture toughness is shown to increase with the fracture velocity. This technique is readily implementable and can be applied to investigating fracture mechanics of other brittle materials.

ACKNOWLEDGMENTS

The authors acknowledge the support by NSERC/Discovery Grant No. 72031326. One of the authors (R. C.) is partially supported by China Scholarship Council for his research in University of Toronto.

REFERENCE:

- [1] Z.X. Zhang, S.Q. Kou, J. Yu, Y. Yu, L.G. Jiang, P.A. Lindqvist, Effects of loading rate on rock fracture, *Int J Rock Mech Min Sci* 36 (5) 1999 597-611
- [2] Z.X. Zhang, S.Q. Kou, L.G. Jiang, P.A. Lindqvist, Effects of loading rate on rock fracture: fracture characteristics and energy partitioning, *Int J Rock Mech Min Sci* 37 (5) 2000 745-762
- [3] W. Böhme, J.F. Kalthoff, The behavior of notched bend specimens in impact testing, *Int J Fract* 20 (4) 1982 R139-R143
- [4] H. Maigre, D. Rittel, Dynamic fracture detection using the force-displacement reciprocity: Application to the compact compression specimen, *Int J Fract* 73 (1) 1995 67-79
- [5] D.M. Owen, S. Zhuang, A.J. Rosakis, G. Ravichandran, Experimental determination of dynamic crack initiation and propagation fracture toughness in thin aluminum sheets, *Int J Fract* 90 (1-2) 1998 153-174
- [6] T. Weerasooriya, P. Moy, D. Casem, M. Cheng, W. Chen, A four-point bend technique to determine dynamic fracture toughness of ceramics, *J Am Ceram Soc* 89 (3) 2006 990-995
- [7] A. Bertram, J.F. Kalthoff. Crack propagation toughness of rock for the range of low to very high crack speeds. In: Buchholz FG, Richard HA, Aliabadi MH, editors. *Advances in Fracture and Damage Mechanics Key engineering materials*. Uetikon-Zurich: Trans Tech Publications, 2003. p. 423-430.
- [8] L.B. Freund, *Dynamic fracture mechanics*, Cambridge University Press, Cambridge, 1990
- [9] K. Xia, V.B. Chalivendra, A.J. Rosakis, Observing ideal "self-similar" crack growth in experiments, *Eng Fract Mech* 73 (18) 2006 2748-2755
- [10] C.N. Tang, X.H. Xu, A new method for measuring dynamic fracture-toughness of rock, *Eng Fract Mech* 35 (4-5) 1990 783-789
- [11] K.T. Ramesh, N. Kelkar, Technique for the Continuous Measurement of Projectile Velocities in Plate Impact Experiments, *Rev Sci Instrum* 66 (4) 1995 3034-3036
- [12] K.P. Chong, M.D. Kuruppu, New specimen for fracture-toughness determination for rock and other materials, *Int J Fract* 26 (2) 1984 R59-R62
- [13] H. Kolsky, *Stress waves in solids*, Clarendon Press, Oxford, 1953
- [14] D.J. Frew, M.J. Forrestal, W. Chen, Pulse shaping techniques for testing brittle materials with a split Hopkinson pressure bar, *Exp Mech* 42 (1) 2002 93-106
- [15] R.S. Barsoum, Triangular quarter-point elements as elastic and perfectly-plastic crack tip elements, *Int J Numer Methods Eng* 11 (1) 1977 85-98
- [16] N. Iqbal, B. Mohanty, Experimental calibration of stress intensity factors of the ISRM suggested cracked chevron-notched Brazilian disc specimen used for determination of mode-I fracture toughness, *Int J Rock Mech Min Sci* 43 (8) 2006 1270-1276